RSC Advances

PAPER

View Article Online
View Journal | View Issue

Cite this: *RSC Adv.*, 2025, **15**, 38406

Tailoring Janus In_2SeTe monolayers with Al doping: a computational study for NO_x sensing applications

Manik Bala, Md Tawabur Rahman * and Nilachal Goswami

Anthropogenic emissions of harmful gases from fossil fuel combustion and industrial processes require advanced sensing platforms with exceptional sensitivity and selectivity. Herein, we present a comprehensive first-principles study of a Janus In_2SeTe monolayer and its aluminum-doped analogue as multifunctional gas sensors. Using Density Functional Theory (DFT), we examine the adsorption of six common pollutants, including CO, NH_3, CO_2, CH_4, NO, and NO_2 on geometrically optimized surfaces, analyzing adsorption energy, distance, charge transfer, Density of States (DOS), Electron Density Difference (EDD), and recovery time. We further evaluate the resultant changes in electronic band structure, conductivity, optical absorption, refractive index, and spin-resolved DOS. Our results reveal that only NO and NO_2 chemisorb strongly, inducing the highest adsorption energies and shortest distances, while the other gases physiosorbed weakly. The adsorption of NO_x narrows the bandgap by 0.46/0.408 eV (NO/NO_2) and 1.068/0.612 eV (NO/NO_2) for pristine and Al-doped In_2SeTe, respectively, translating into dramatic chemiresistive responses. At the optimized Al-doping level (2.33% Al for NO, 5.5% Al for NO_2), the sensitivity was boosted by a factor of 1.26×10^5 (NO) and 51.6 (NO_2) compared to the pristine In_2SeTe. The optical absorption and refractive index spectra exhibit gas-specific shifts in pristine In_2SeTe for NO and Al-doped In_2SeTe for NO_2, while only NO_x adsorption generates a nonzero magnetic moment, enabling concurrent optical, chemiresistive, and magnetic transduction. The obtained faster recovery time supports real-time and reusable detection of NO_x. Thus, these findings establish Al-doped In_2SeTe as an excellent sensing material for next-generation environmental NO_x sensing.

Received 1st August 2025
Accepted 7th October 2025

DOI: 10.1039/d5ra05591a

rsc.li/rsc-advances

1 Introduction

Toxic gas detection is crucial for safeguarding health, ensuring workplace safety, complying with regulations, protecting the environment, and facilitating prompt emergency actions.[1,2] Furthermore, the world's overpopulation and industrialization are constantly increasing emissions, endangering all life on the planet.[3] The World Health Organization (WHO) estimates that outdoor air pollution frequently contains harmful gases and causes 4.2 million deaths worldwide. In this industrial era, it is necessary to design stable, ultra-fast, precise, and sensitive gas sensors to detect toxic gases at part-per-billion (ppb) concentrations.[4] The sensitivity of conventional Metal Oxide Semiconductor (MOS) devices is restricted at lower concentrations, despite their exceptional sensitivity and selectivity.[5] After the discovery of graphene, the area of two-dimensional (2D) materials has expanded enormously.[6,7] Their high surface area and excellent electrical and chemical characteristics make 2D materials highly promising for gas substance detection.[8] The first-principles investigations are essential for developing gas sensor research because they are crucial in forecasting gas adsorption behavior in emerging 2D materials.[9,10]

In recent years, the layered transition metal dichalcogenides (TMDs) have garnered a lot of interest due to their fascinating physical and chemical properties.[11,12] Notable features include topological superconductivity, an indirect-to-direct bandgap crossover, valley-selective optical stimulation, a layer-dependent tunable bandgap, out-of-plane piezoelectric polarization, and a significant Rashba effect due to their out-of-plane asymmetries.[4,13] MoSSe, one of the Janus TMDs, has already been developed experimentally using chemical vapor deposition (CVD).[14,15] Jin *et al.* demonstrated the Janus MoSSe, which has shown promise for creating ultrahigh-sensitivity nanoscale sensors with enhanced sensitivity to NH_3 and NO_2 due to the inner electric field and tunable selectivity resulting from the Janus structure.[16] P. Yu *et al.* employed a Pd-doped Janus HfSeS monolayer as an ultrahigh-sensitive gas sensing material for reversible detection of NO.[17] Very recently, the electronic structure, optical, and thermoelectric properties of a new 2D Janus telluride (In_2SeTe) monolayer, the Janus In_2SeTe monolayer with asymmetric Se/Te surfaces, have been investigated.[18] However, the gas adsorption properties of In_2SeTe monolayers remain unexplored.

This study utilized DFT calculations to investigate the gas-sensing characteristics of both pristine and aluminum-doped

Department of Electrical and Electronic Engineering, Khulna University of Engineering & Technology, Khulna-9203, Bangladesh. E-mail: tawabur@eee.kuet.ac.bd

In_2SeTe monolayers toward NH_3, CO_2, CO, NO, NO_2, and CH_4. Al was chosen as a substitutional dopant due to its similar atomic radius to host atoms, ensuring structural stability, and its trivalent nature, which modulates the electronic structure and enhances charge redistribution. Its higher electropositivity strengthens interactions with electronegative gases. Being abundant, low-cost, lightweight, and non-toxic, Al offers both electronic advantages and practical sustainability for gas-sensing applications. The initial assessment focused on adsorption strength, determined by adsorption energy and height of the gas molecules on the Se-terminated surface of the monolayers. Key structural and electronic properties—including binding energy, charge transfer, sensitivity, recovery time, and EDD—were systematically analyzed. Results indicated significantly stronger interactions between the monolayer and NO/NO_2 compared to the other gases. Additionally, DOS analysis provided insight into the role of atomic orbitals in gas adsorption. The pristine In_2SeTe monolayer exhibited high sensitivity values of 7.25×10^5 for NO and 2.65×10^5 for NO_2. These sensing performances were further enhanced through 2.33% Al doping, which led to substantial sensitivity improvements by factors of 1.26×10^5 for NO and 51.58 for NO_2 relative to the undoped system. The effect of aluminum concentration on sensing performance was also evaluated, revealing optimal doping levels of 2.33% for NO and 5.5% for NO_2. Importantly, the recovery times for both pristine and Al-doped monolayers remained within feasible limits, supporting real-time, repeatable gas detection. Deviations from these doping levels resulted in a noticeable drop in sensitivity, highlighting the importance of maintaining a balance between structural integrity and electronic responsiveness. The optical analysis further demonstrated selective gas detection capabilities—pristine In_2SeTe was responsive to NO, while Al-doped In_2SeTe showed specificity toward NO_2. Moreover, only NO_x gases induced magnetism in both systems, enabling their use as magnetic sensors exclusively for NO_x detection. Overall, Al doping significantly improved the electronic, optical, and chemical sensing performance of the In_2SeTe monolayer. These enhancements establish Al-doped In_2SeTe as a highly effective material for next-generation gas sensors, offering excellent selectivity, sensitivity, and reliability for detecting hazardous environmental gases.

The material's high sensitivity and selectivity toward NO_x make it an ideal candidate for urban air quality monitoring, such as in roadside, playground, and smart city nodes, where accurate and reliable NO_2 detection is essential for protecting public health. Its robust reaction to NO and NO_2 indicates potential for usage in onboard diagnostics and selective catalytic reduction (SCR) systems for vehicle exhaust sensors. Applications in continuous emissions monitoring and fence-line surveillance at industrial sites are supported by exceptional room-temperature performance. Use of tunnel and parking area safety and ventilation systems is made possible by quick reaction and recovery. Its NO sensitivity also indicates the possibility of non-invasive monitoring of exhaled nitric oxide (FeNO), a biomarker for asthma treatment, in medical devices.

2 Computational methods

DFT was employed in this study, and all calculations were performed using the DMol^3 modules integrated into the Materials Studio platform.[19] Initially, a supercell (3×3) of the In_2SeTe monolayer was created. Then, the bulk In_2SeTe crystal was cleaved, and a 25 Å vacuum zone was included to eliminate spurious interactions with periodic images, ensuring sufficient accuracy for electronic and optical property calculations.[20] The DMol^3 module optimized the In_2SeTe monolayer until the energy converged to precision values of 1.0×10^{-6} Ha. The value of the force limit was 1.0×10^5 Ha per Å. The DSPP (DFT Semi-core Pseudo Potential) approach incorporated relativistic corrections into the core treatment. Smearing was adjusted to 0.005 Ha to expedite convergence. A Monkhorst Pack *k*-point set of $5 \times 5 \times 1$ was selected for geometry optimization and electronic structure calculations. A Double Numerical Polarized Plus (DNP+) basis set was chosen for the optimization[9] The value of the Global Orbital cut-off was 5.0 Å. GGA (Generalized Gradient Approximation) and PBE (Perdew Burke Ernzerhof) functional theory were used for computational efficiency. Using the GGA and GGA + SOC (Spin-Unrestricted) methods, we have calculated the electronic properties of NO and NH_3 adsorption, revealing that the interplay between angular momentum and orbital angular momentum causes the splitting of energy bands.[21,22] The HSE06 functional, which combines Heyd, Scuseria, and Ernzerhof, is quite close to the experimental band gap values. However, the change in the band gap is more important for sensing applications than the absolute value.[22,23] After geometry optimization, various parameters, including bond length, band structure, DOS, and Hirshfeld charge analyses, were calculated. Adsorption energy (E_{ad}) was defined as follows:[24,25]

$$E_{ad} = E_{(monolayer+gas)} - E_{(monolayer)} - E_{(gas)} \quad (1)$$

The energy of the monolayer following gas adsorption is denoted by $E_{(monolayer+gas)}$, the energy of the monolayer itself is denoted by $E_{(monolayer)}$, and the total energy of the sole gas layer is denoted by $E_{(gas)}$. Eqn (2) was used to determine the amount of charge transfer during the adsorption phase.

$$\Delta Q = Q_{ads} - Q_{iso} \quad (2)$$

The total charge of the gas molecule before and after adsorption is indicated by Q_{iso} and Q_{ads}, respectively. The energy gap can be used to assess the material's change in conductivity. In this instance, E_{HOMO} stands for the energy of the highest occupied molecular orbit, whereas E_{LUMO} indicates the energy of the lowest unoccupied molecular orbit. The structure's energy gap is shown by

$$E_g = E_{LUMO} - E_{HOMO} \quad (3)$$

The charge density difference in the adsorption process, $\Delta\rho$, was defined using eqn (4).

$$\Delta\rho = \rho_{(gas+m)} - \rho_m - \rho_{gas} \quad (4)$$

ρ_{total}, ρ_m, and ρ_{gas} denote the charge densities after gas adsorption, of the pristine/Al-doped structure, and of the isolated gas molecule, respectively. The conductivity and band gap of a material can be found in the following equation:[26,27]

$$\sigma = A\exp\left(-\frac{E_g}{2k_BT}\right) \quad (5)$$

Here, A is the proportionality constant, E_g is the band gap, and T is the temperature in Kelvin.

The relationship between chemiresistive sensitivity and conductivity is defined by:

$$\%S\left(\frac{\delta\sigma}{\sigma}\right) = \frac{\exp\left(-\frac{E_g(\text{adsorbed})}{2k_BT}\right) - \exp\left(-\frac{E_g(\text{pristine})}{2k_BT}\right)}{\exp\left(-\frac{E_g(\text{pristine})}{2k_BT}\right)} \times 100 \quad (6)$$

The time required for gas molecules to desorb naturally from the surface of the sensing material is called the recovery time. To determine the recovery time, the Vant Hoff Arrhenius equation was applied, as shown below.[4,28]

$$\tau = {\nu_0}^{-1}\exp\left(-\frac{E_{ad}}{k_BT}\right) \quad (7)$$

The attempt frequency, represented as ν_0, is commonly assumed to be 10^{12} s^{-1} for SO_2, as reported in previous research.[9] For all other gases, the same value can be applied.

For pristine In_2SeTe, In (on top of the In atom), Se (on top of the Se atom), Te (on top of the Te atom), bridge (on top of the In–Se bonds), and bridge (on top of the In–Te bonds) are the five initial adsorption sites that were chosen, as shown in Fig. 1(a). Similarly, for Al-doped In_2SeTe, In (on top of the In atom), Se (on top of the Se atom), Te (on top of the Te atom), Al(on top of the Al atom), bridge (on top of the In–Se bonds), and bridge (on top of the In–Te bonds) are the six initial adsorption sites that were chosen, as shown in Fig. 1(b). Lastly, the pristine and Al-doped In_2SeTe monolayer's capacity for gas sensing was investigated, considering the sensing parameters of conductivity, refractive index, magnetic moment, and recovery time.

3 Results and discussion

3.1 Parameter optimization of pristine and Al-doped In_2SeTe monolayer

This study systematically investigates the structural and electronic properties of pristine and Al-doped In_2SeTe monolayers, with a particular focus on their response to gas adsorption. Both configurations exhibit a low-buckled structure, with lattice constants of 4.0381 Å for pristine and 4.054 Å for Al-doped In_2SeTe, aligning well with previous reports based on PBE-level calculations.[18] A 3 × 3 supercell was employed to model the local atomic interactions with gas molecules. As shown in Fig. 1, the atomic arrangement along the Z-axis follows a Se–In–In–Te sequence, indicating that indium atoms are sandwiched between selenium and tellurium layers. The introduction of Al slightly alters the local geometry. In the pristine structure, the In–In, In–Se, and In–Te bond lengths are 2.768 Å, 2.684 Å, and

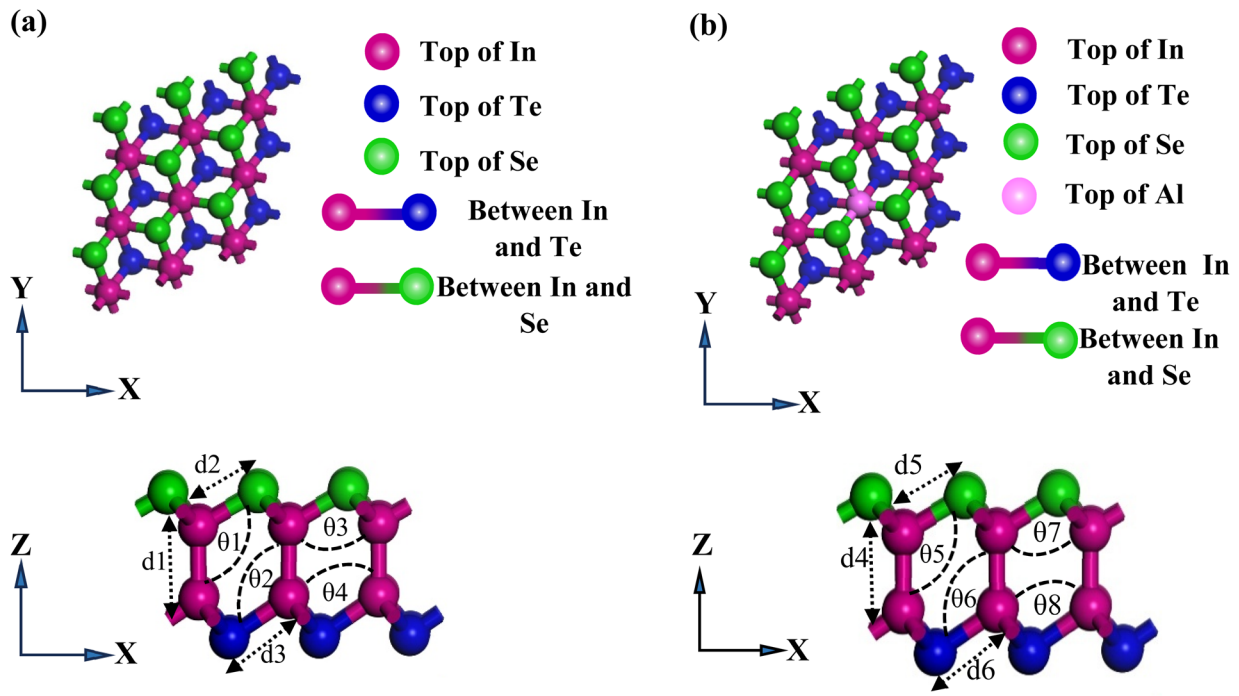

Fig. 1 (a) Top view, and side view of the pristine Janus In_2SeTe structures with bond length, bond angles, and five distinct adsorption sites. (b) Top view and side view of the Al-doped Janus In_2SeTe structures with bond length, bond angles, and six distinct adsorption sites.

2.815 Å, respectively, while in the doped structure, these values shift to 2.767 Å, 2.712 Å, and 2.809 Å. Corresponding changes in bond angles and structural thickness (from 5.40 Å to 5.34 Å) reflect the subtle influence of Al incorporation. Phonon dispersion spectra (Fig. 2(a) and (d)) for both systems show the absence of imaginary frequencies, confirming their dynamic stability. Each unit cell, comprising four atoms, exhibits twelve phonon branches—three acoustic and nine optical—with linear acoustic modes near the Γ-point and a phonon gap separating degenerate and non-degenerate modes, characteristics typical of two-dimensional materials. Electronic band structure analysis (Fig. 2(b) and (e)) reveals that both pristine and Al-doped monolayers are direct bandgap semiconductors with their valence band maximum (VBM) and conduction band minimum (CBM) located at the Γ-point. The calculated band gaps are 1.192 eV for pristine and 1.109 eV for Al-doped In_2SeTe, indicating a slight reduction in band gap due to doping while preserving the semiconducting nature of the material. In Fig. 2(c), the projected density of states (PDOS) of the pristine In_2SeTe features a pronounced Te-s peak at −15 eV, indicating a localized deep valence state. Near the Fermi level, in p, Se p, and Te p orbitals dominate and strongly hybridize, driving both bonding and electronic behavior, and they also extend modestly into the conduction band. All other s and d orbitals are negligible, underscoring p-orbital interactions as the key determinant of In_2SeTe's electronic properties. In the Al-doped In_2SeTe monolayer, the PDOS still features a deep, intense Te s peak at −15 eV, indicating that the core valence band structure remains intact, as displayed in Fig. 2(f). Doping introduces new Al-derived features: a small Al-s peak appears around −13 eV, and Al-p states emerge just below and slightly above the Fermi level (0 eV), indicating that Al partially hybridizes with the host p orbitals. The dominant In-p, Se-p, and Te-p contributions near Ef are preserved but become slightly redistributed by the added Al-p density, leading to a modest increase in total DOS at the valence-band edge. Above E_f, faint Al-p weight extends into the conduction band, suggesting that Al doping can enhance carrier availability and subtly narrow the band gap without disrupting the principal p-orbital framework of In_2SeTe. Table SI provides the structural properties of pristine and Al-doped In_2SeTe, covering bond lengths, bond angles, dynamic stability, band gap values, and the positions of VBM and CBM. Table SII presents a comparison of the computed lattice constant, thickness, bond lengths, and PBE band gap with previously reported results. The strong agreement confirms the reliability of our calculations, while slight deviations are linked to variations in exchange–correlation functionals, computational parameters, and dispersion treatments.[18,29–31]

3.2 Adsorption configurations of different gases on pristine and Al-doped In_2SeTe monolayer

Geometry optimization was performed after placing the gas molecule on the monolayer with a distinct adsorption distance. The same gas molecule can exhibit different characteristics depending on the specific adsorption site, adsorption distance, and orientation of the molecule. Some gas molecules tend to adsorb parallel to the monolayer, while others like to orient

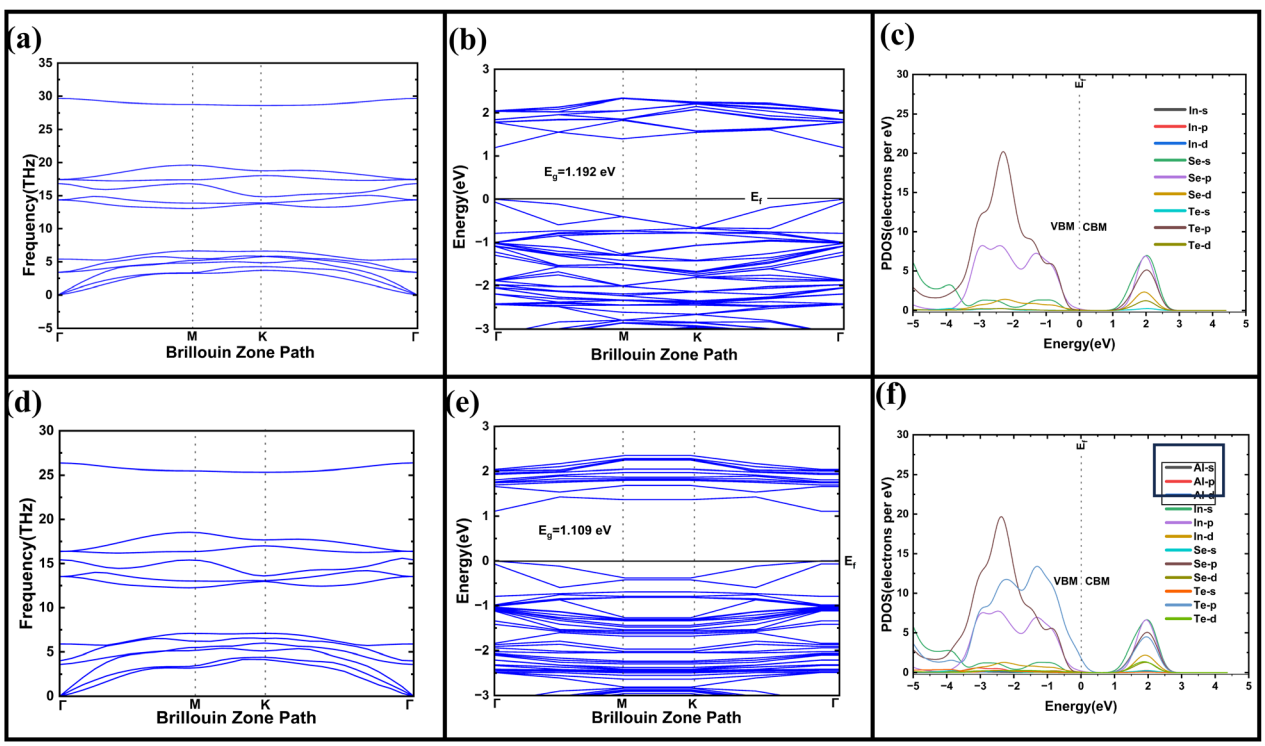

Fig. 2 (a) Phonon frequency, (b) Band structure, and (c) PDOS of pristine In_2SeTe monolayer, (d) phonon dispersion, (e) Band structure, and (f) PDOS of pristine Al-doped In_2SeTe monolayer.

vertically or obliquely. Adsorption is generally referred to as chemisorption if the absolute value of the adsorption energy is greater than 0.5 eV.[32] The types and combinations of adsorption are represented in detail in the related figures in the following section.

3.2.1 NH_3. Following NH_3 adsorption on pristine In_2SeTe, the adsorption energy value was around −0.20589 eV, indicating a moderate interaction between NH_3 gas and the monolayer. The NH_3 molecule preferentially adsorbs at the top of the Te atom with an adsorption distance of 2.86 Å, as illustrated in Fig. S1(a), and the value of the charge transfer is measured at 0.0934|e| from In_2SeTe monolayer to NH_3 can be observed in EDD Fig. S2(a). The calculated adsorption energy and substantial charge transfer indicate that NH_3 undergoes physisorption on the In_2SeTe monolayer. The change in band gap is about −0.009 eV, which is almost negligible. Fig. 8(a) reveals that NH_3 has a negligible impact on the electronic characteristics of In_2SeTe monolayers. As seen in Fig. 7(a), the N and H atoms of NH_3 molecules contribute very little to the DOS. As it was doped with Al and eventually NH_3 was adsorbed on the monolayer, the adsorption behavior remained the same, with only a slight variation from the pristine state. The adsorption energy value was around −0.225 eV, suggesting a stronger interaction between the gas molecule and the doped surface compared to the pristine configuration. In Fig. 3(a), the NH_3 molecule was adsorbed on top of the Te atoms with an adsorption distance of 2.94 Å from the surface, with a charge transfer value of 0.097|e|, as presented in EDD Fig. 4(a). Although NH_3 is still physisorbed on the Al-doped In_2SeTe, these findings indicate an enhancement in adsorption behavior after Al doping, marked by increased adsorption energy and charge transfer. Additionally, after doping, the insignificant change in bandgap increased to −0.013 eV, indicating a negligible decrease in conductivity after NH_3 adsorption.

3.2.2 CH_4. Upon adsorption of CH_4 on pristine In_2SeTe, the interaction becomes comparatively weaker, with an adsorption energy of −0.11 eV and a relatively large adsorption distance of 3.27 Å portrayed in Fig. S1(b) as CH4 is adsorbed on the top of the In–Se bridge as its favorable adsorption sites, followed by a minimal charge transfer of 0.064|e|.The substantial charge transfer can also be confirmed by the charge accumulation and depletion in Fig. S2(b). The bandgap change is considerably lower at −0.024 eV, which can be neglected. PDOS analysis reveals that the C and H atoms of CH_4 contribute insignificantly to the DOS near the Fermi level, indicating limited orbital hybridization. After Al doping, the adsorption energy increases to −0.129 eV, and the distance decreases to 3.062 Å and adsorbs on top of the Al–Se bridge, while charge transfer falls to 0.049|e|, confirmed by Fig. 3(b) and 4(b). The bandgap difference still remains unnoticeable at −0.005 eV. Due to this low adsorption energy and low charge transfer, CH_4 is physisorbed on both pristine and Al-doped In_2SeTe monolayer. As the bandgap change is insignificant, the conductivity remains unchanged after gas adsorption, resulting in no change in sensitivity. Due to these reasons, CH_4 gases cannot be detected through pristine/Al-doped In_2SeTe.

3.2.3 CO_2. CO_2 portrays a very mild interaction with the pristine In_2SeTe monolayer, as reflected by its low adsorption energy of −0.15 eV and a relatively large distance of 3.39 Å from the surface. CO_2 gas molecule is adsorbed on top of the In–Te bridge as a favorable adsorption site, displayed in Fig. S1(c). The bandgap remains almost unbothered, shifting by just −0.077 eV, and the charge transfer is minimal at 0.039|e|—all pointing to a negligible effect on the electronic properties of the material shown in Fig. S2(c). This is further supported by the PDOS analysis, which reveals that the O-p states from the CO_2 molecule contribute minimally near the Fermi level. However, the picture changes significantly when the surface is doped with Al. The CO_2 molecule moves slightly closer, sitting on the top of the Se atoms with an adsorption distance of 3.31 Å, and the adsorption energy becomes noticeably more negative at −0.196 eV with the adsorption configuration shown in Fig. 3(c), indicating a stronger attraction. Charge transfer increases to 0.041|e|, suggesting a more pronounced interaction. The substantial charge transfer can also be confirmed by the charge accumulation and depletion in Fig. 4(c). The PDOS now clearly shows hybridization between the Se-p orbitals of the doped monolayer and the O-p and C-p orbitals of CO_2, even though the bandgap change, at −0.004 eV, is still relatively balanced. Due to this low adsorption energy and low charge transfer, CO_2 is physisorbed on both pristine and Al-doped In_2SeTe monolayer.

3.2.4 CO. As the interaction between CO and pristine In_2SeTe monolayer takes place, it is observed that the adsorption is insignificant, marked by an adsorption energy of −0.06 eV. CO adsorbed just above the In atom, having the highest adsorption distance of 3.403 Å between the molecule and the surface among all other gases displayed in the adsorption configuration in Fig. S1(d). The charge transfer was very low at 0.014|e|, confirmed by a very low charge accumulation on the CO atom shown in Fig. S2(d), and the bandgap deviates only slightly by 0.003 eV. PDOS analysis exhibits that the C-p and O-p orbitals from CO make only a faint contribution near the Fermi level, indicating limited electronic interaction. After Al doping, the adsorption energy becomes more negative, at −0.135 eV, and CO settles even closer to the surface, adsorbed on the top of the Al atom with a distance of 3.8 Å, as it's a highly favorable adsorption site as displayed in Fig. 3(d). The charge transfer nearly doubles to 0.028|e| can be observed in Fig. 4(d), and the bandgap change becomes much more promising at −0.006 eV. Even though Al doping occurs, there is no noticeable change in the electronic properties; it doesn't detect CO gases selectively. With these trivial adsorption energies and low charge transfer, CO gas molecules undergo physisorption in both pristine In_2SeTe and Al-doped In_2SeTe

3.2.5 NO. The interaction is significantly strong due to the adsorption of NO on the In–Se bridge of the pristine In_2SeTe monolayer, with an adsorption energy of −0.751 eV and the molecule settling at least adsorption distance of 2.17 Å from the surface, displayed in the adsorption configuration Fig. S1(e). The charge transfer is 0.074|e| confirmed by a large charge accumulation on NO in Fig. S2(e), and the bandgap change is exceptional, −0.460 eV. PDOS analysis reveals that the O-p

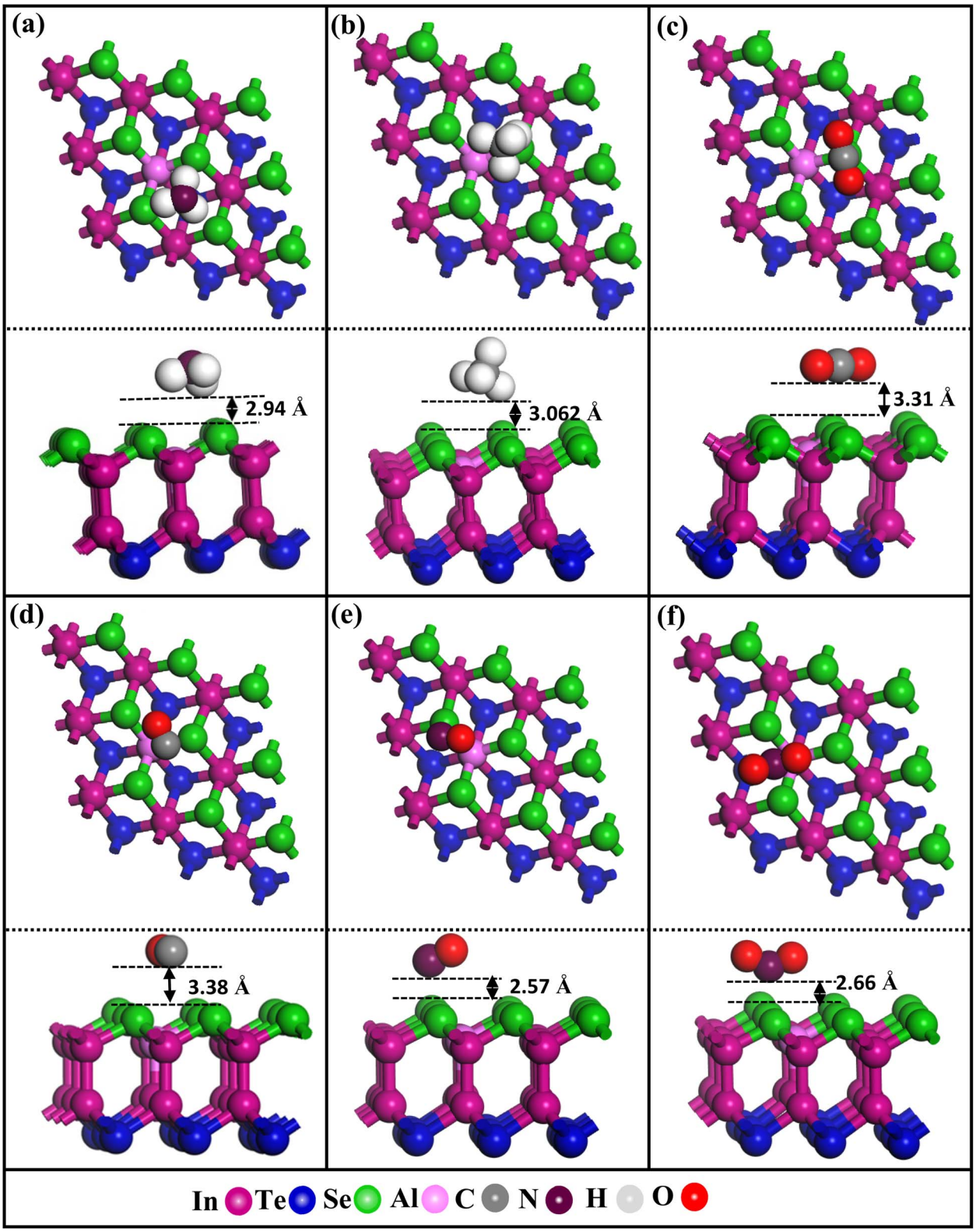

Fig. 3 Top view and side view of Al-doped In_2SeTe monolayer after (a) NH_3, (b) CH_4, (c) CO_2, (d) CO, (e) NO, and (f) NO_2 gas adsorption.

orbitals contribute highly near the Fermi level, indicating stronger electronic interaction. However, after doping the surface with Al, the adsorption characteristics change dramatically. The adsorption energy becomes significantly more negative at −0.774 eV, and NO is adsorbed on top of the Al–Se bridge with an adsorption distance of 2.57 Å, as displayed

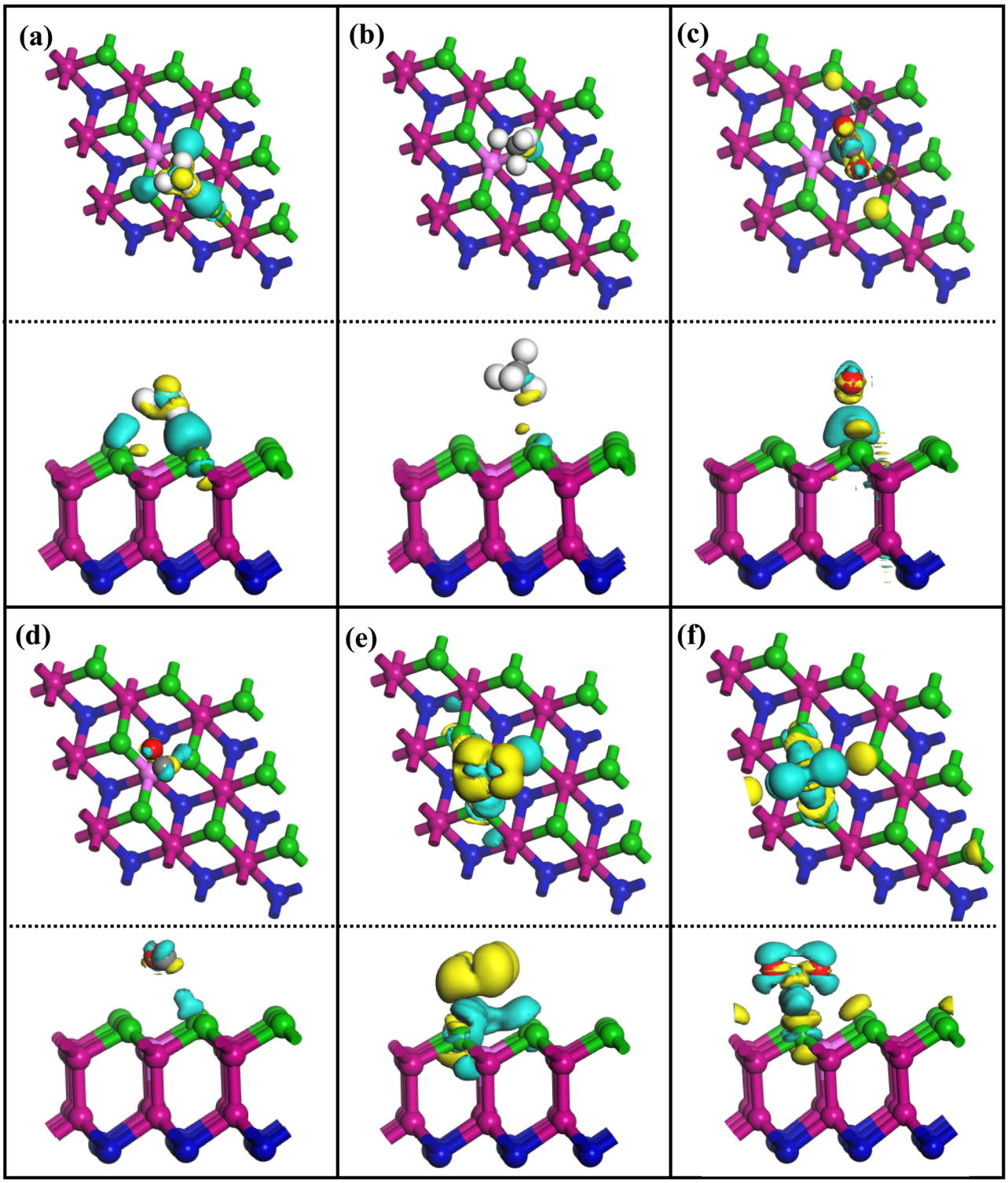

Fig. 4 Top view and side view of charge density of Al-doped In_2SeTe monolayer after (a) NH_3, (b) CH_4, (c) CO_2, (d) CO, (e) NO, and (f) NO_2 gas adsorption, where cyan color indicates charge accumulation and yellow color indicates charge depletion.

in Fig. 3(e). Charge transfer increases to 0.082|e|, and the bandgap change jumps to −1.068 V, a maximum in comparison to other gases, signifying a much greater impact on the material's electronic properties. The substantial charge transfer can also be confirmed by the charge accumulation and depletion in Fig. 4(e). With these high adsorption energies and substantial charge transfer, NO gas molecules undergo chemisorption in both pristine In_2SeTe and Al-doped In_2SeTe. The PDOS now displays intense N-p and O-p peaks near the Fermi level, pointing to vigorous orbital mixing between NO and the Al-

doped monolayer. In summary, while the pristine surface illustrates high sensitivity to NO, Al doping greatly amplifies both the strength of adsorption and its electronic consequences, like sensitivity, charge transfer, recovery time, *etc.*, making the doped material far more effective for NO detection.

3.2.6 NO_2. For NO_2 adsorbed on top of the In–Te bridge, the pristine In_2SeTe monolayer already demonstrates a relatively strong interaction, with an adsorption energy of −0.589 eV, and a short adsorption distance of 2.75 Å can be observed in the top view and side view of the adsorption configuration in Fig. S1(f). Besides, the charge transfer is 0.066|e|, and the bandgap change is −0.408 eV. The charge transfer can also be observed in EDD Fig. S2(f). There is a charge accumulation on NO_2. PDOS analysis reveals only marginal contributions from the N-2p orbitals, indicating that, although the interaction is stronger than for some other gases, its effect on electronic properties remains limited. The situation becomes very promising with Al doping: the adsorption energy plunges to −0.701 eV, and NO_2 sits even closer to the surface at the Al–Te bridge with an adsorption distance of 2.66 Å in Fig. 3(f). The charge transfer becomes 0.08|e|, which can also be confirmed by the charge accumulation and depletion in Fig. 4(f) with a huge charge accumulation onto the O atoms of NO_2. Additionally, the bandgap change reaches a substantial −0.612 eV. With these high adsorption energies and substantial charge transfer, NO_2 gas molecules undergo chemisorption in both pristine In_2SeTe and Al-doped In_2SeTe. The PDOS now reveals dominant N-p and O-p peaks, strongly hybridized with Al-p states, confirming robust orbital mixing and a pronounced alteration of the electronic structure. Although pristine In_2SeTe itself is highly sensitive to NO_2, the sensitivity dramatically enhances through Al doping, making the Al-doped In_2SeTe monolayer selectively detect NO_2 gas molecules.

3.3 Electronic structures and atomic contributions after gas adsorption

It is anticipated that the electrical structures of Al-doped In_2SeTe monolayer and pristine In_2SeTe monolayer would change when gas molecules are present. Thus, band structures and orbital- PDOS were calculated. The band structures of every gas-adsorbed system are displayed in Fig. 5 and 6 for both pristine and Al-doped In_2SeTe systems. NH_3 and CO have a negligible effect on the electronic band structure characteristics of pristine/Al-doped In_2SeTe monolayers, as shown in Fig. 5(a) and 6(a). The observed change in the band gap was negligible. As shown in Fig. 7(a) and (d) for pristine In_2SeTe and in Fig. 8(a) and (d) for Al-doped In_2SeTe, the nitrogen and hydrogen atoms in NH_3 molecules and the carbon and oxygen atoms in CO molecules make minimal contributions to the PDOS. As a result, there was no noticeable change in the electronic properties. For pristine In_2SeTe, the band gap changed significantly by 0.460 eV and 0.408 eV, respectively, as a result of NO and NO_2 being adsorbed onto the In_2SeTe monolayer. The PDOS, demonstrated in Fig. 7(e) and (f), shows distinct evidence of hybridization between the nitrogen and oxygen atoms in NO_x and the surface atoms of In_2SeTe when NO_x molecules are adsorbed onto the In_2SeTe monolayer. This suggests that these atoms are actively participating in the electronic structure near the edges of the conduction and valence bands. With NO_x adsorption, the PDOS displays strong and sharp peaks for the O-

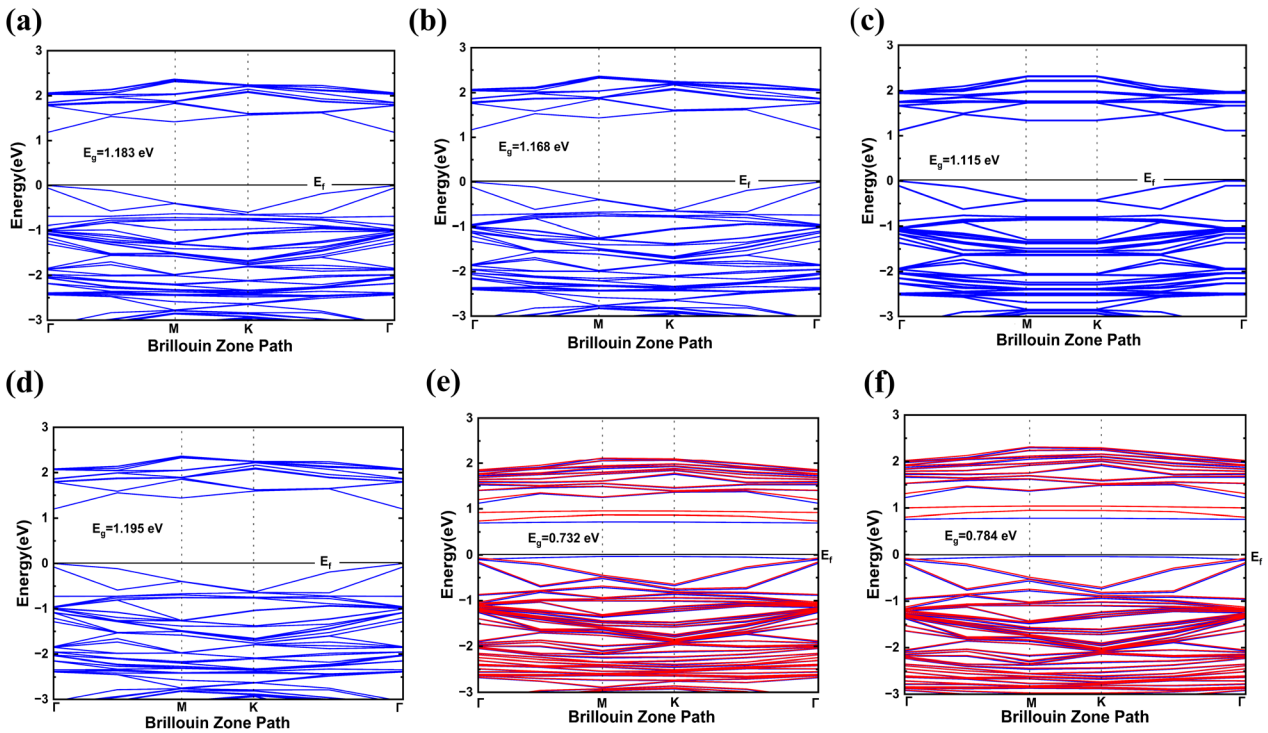

Fig. 5 Band structure of In_2SeTe monolayer after (a) NH_3, (b) CH_4, (c) CO_2, (d) CO, (e) NO, and (f) NO_2 gas adsorption.

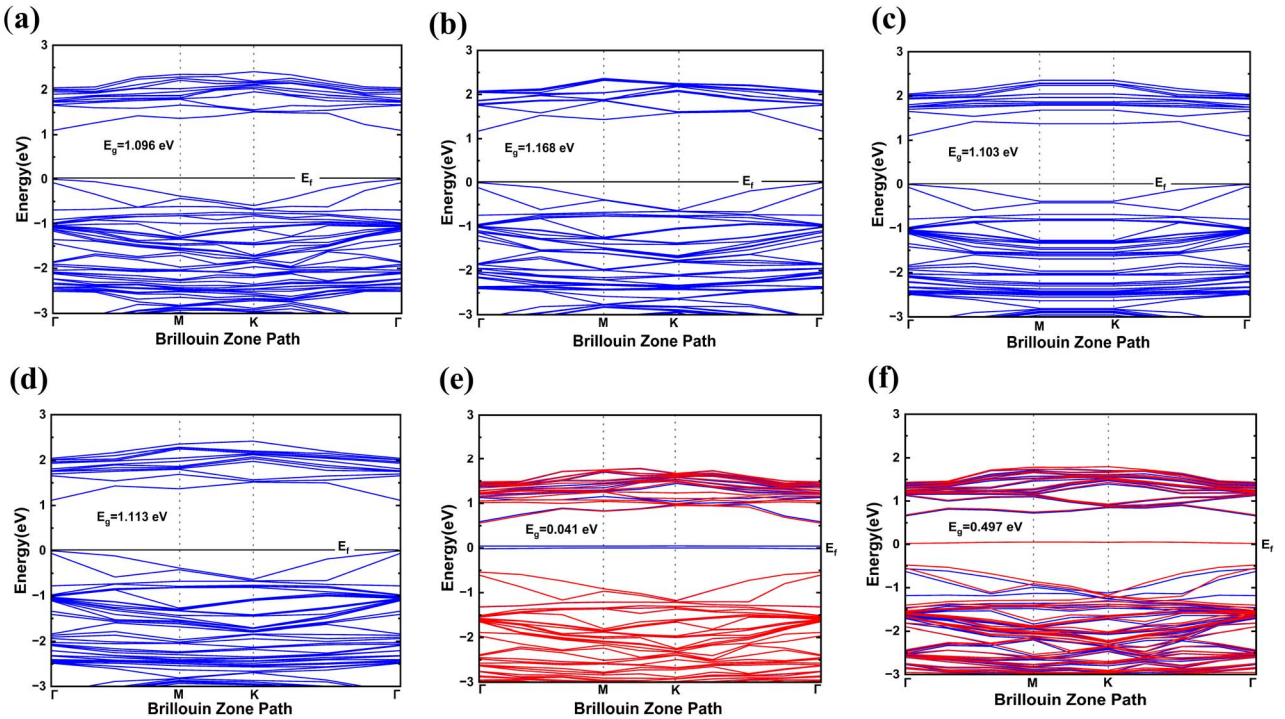

Fig. 6 Band structure of Al-doped In_2SeTe monolayer after (a) NH_3, (b) CH_4, (c) CO_2, (d) CO, (e) NO, and (f) NO_2 gas adsorption.

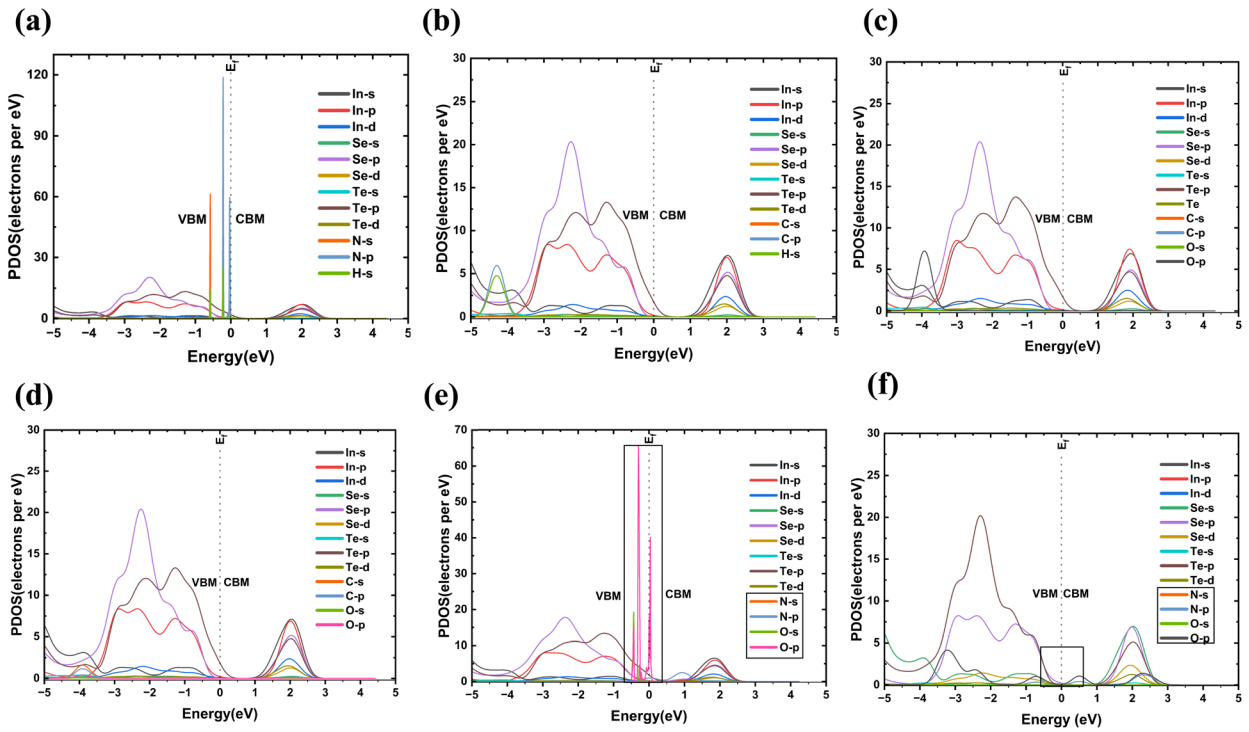

Fig. 7 PDOS of (a) NH_3, (b) CH_4, (c) CO_2, (d) CO, (e) NO, and (f) NO_2 gases adsorbed on In_2SeTe monolayer.

p and N-p orbitals of NO_x, especially in the energy range close to the Fermi level (from 0 to 1.5 eV). These pronounced features are a clear sign of vigorous mixing between the orbitals of NO_x and those of the In_2SeTe substrate, particularly with the p orbitals of selenium and tellurium. This hybridization leads to the appearance of entirely new electronic states within the band gap region, near the Fermi level. At the same time, the main features of the In-d and Se-p orbitals in the host material remain

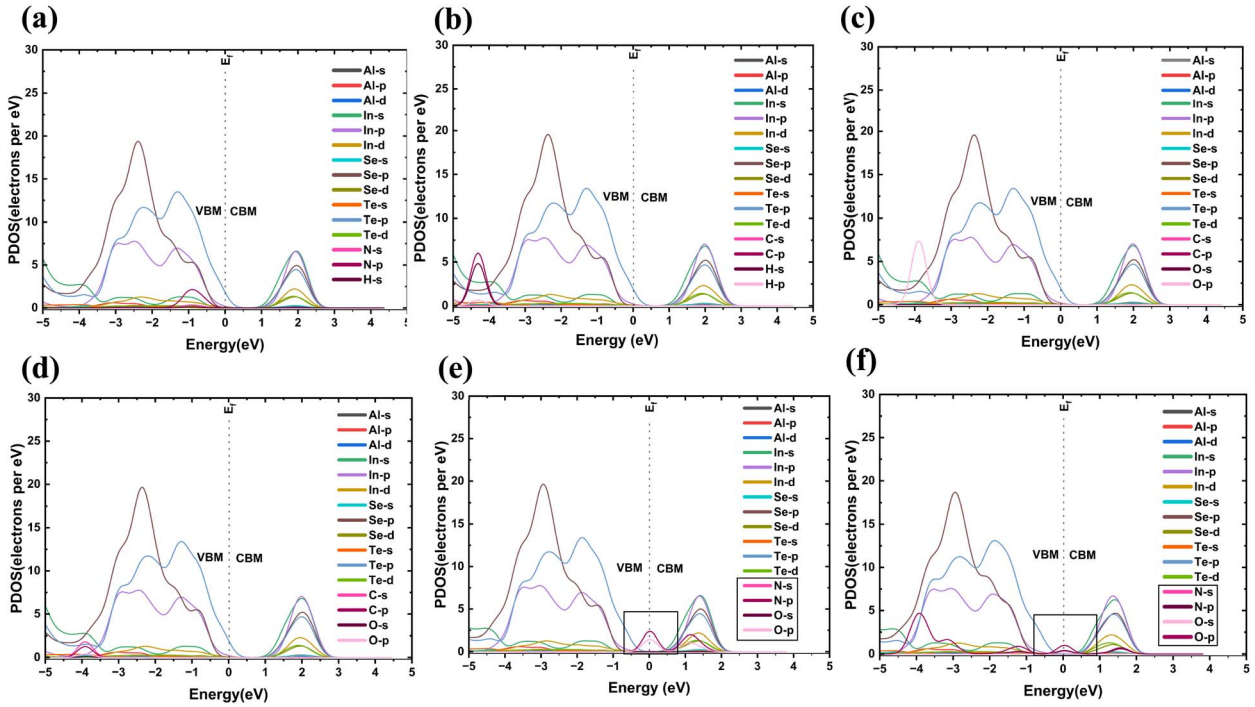

Fig. 8 PDOS of (a) NH_3, (b) CH_4, (c) CO_2, (d) CO, (e) NO, and (f) NO_2 gases adsorbed on Al-doped In_2SeTe monolayer.

mostly unchanged. The strong interaction between NO_x and the In_2SeTe monolayer, as reflected in both the PDOS and the significant changes in electronic properties, highlights the sensitivity of this material in detecting NO_x molecules. Now, for Al-doped In_2SeTe, the electronic bandgap drops more rapidly than pristine In_2SeTe after NO and NO_2 adsorption by a value of 1.068 eV and 0.612 eV, respectively, observed in Fig. 6(e) and (f). From Fig. 8(e) and (f), a stronger hybridization took place among N-p, O-p, Al-p, and Se-p orbitals near the Fermi level than in pristine In_2SeTe, resulting in a new state almost near zero energy level (0–0.5 eV). As a result, the band gap shrinks noticeably.

Additionally, a significant change in the band diagram leads to a corresponding change in the material's conductivity. A significant amount of deflection in the conductivity of the Al-doped In_2SeTe monolayer is responsible for the material's sensitivity towards different gases. One of its capabilities is that of a chemiresistive gas sensor. For both CH_4 and CO_2 adsorption on the pristine/Al-doped In_2SeTe monolayer, the PDOS, illustrated in Fig. 7(b, c) and 8(b, c), exhibits that the C, O, and H orbitals from these molecules contribute only minimally near the Fermi level, with no significant new peaks or strong hybridization observed. As a result, the electronic structure of pristine/Al-doped In_2SeTe remains unchanged mainly after adsorption, and the band gap (Fig. 5(b, c) and 6(b, c)) shows only a negligible variation. These findings indicate that both CO_2 and CH_4 interact very weakly with the pristine/Al-doped In_2SeTe surface, causing little to no modification in its electronic properties, which highlights the material's selectivity and its limited sensitivity to these gases.

3.4 Effect of Al-doping on In_2SeTe for gas sensing

Fig. 9 indicates the effect of Al doping on the electronic and sensing properties of In_2SeTe to NO and NO_2 detection. After observing Fig. 9(a), which depicts how the change in bandgap deviates with various doping percentages, it can be asserted that at 2.77% percent doping of In_2SeTe monolayer with Al atom NO gas, the highest amount of bandgap change (1.068 eV) in comparison to the other doping percentages. Then, eventually, for NO, as the doping percentage is increased, the change in bandgap reduces and reaches a value of 0.722 eV at 11.11% doping. On the contrary, for NO_2, the change in bandgap (0.683 eV) is highest at 5.5% of doping. Now, as we move along, Fig. 9(b) demonstrates the change of logarithmic sensitivity with increasing doping percentage. Along with that, with further observation, the study revealed that at 2.77% NO showed the highest amount of logarithmic sensitivity (10.962), and as the doping percentage rose, logarithmic sensitivity reduced, indicating that as the doping percentage increases, the sensing capability reduces. Adding to the study, the logarithmic sensitivity (7.731) of NO_2 was highest at 5.5% doping of Al in the In_2SeTe monolayer. Furthermore, for 8.33% and 11.11% doping, the logarithmic sensitivity (1.98, 1.99, respectively) was reduced dramatically. From the above explanation, it can be deduced that for NO 2.77% and for NO_2 5.5% doping is ideal to have the maximum amount of sensing performance from Al-doped In_2SeTe monolayer. All these data have been inserted into Table SIII to identify the optimum doping percentage.

Table 1 summarizes the adsorption energy (E_{ad}), bandgap (E_g), bandgap change(ΔE_g), adsorption distance (D), and Hirshfeld charge transfer (ΔQ) of the most energetically

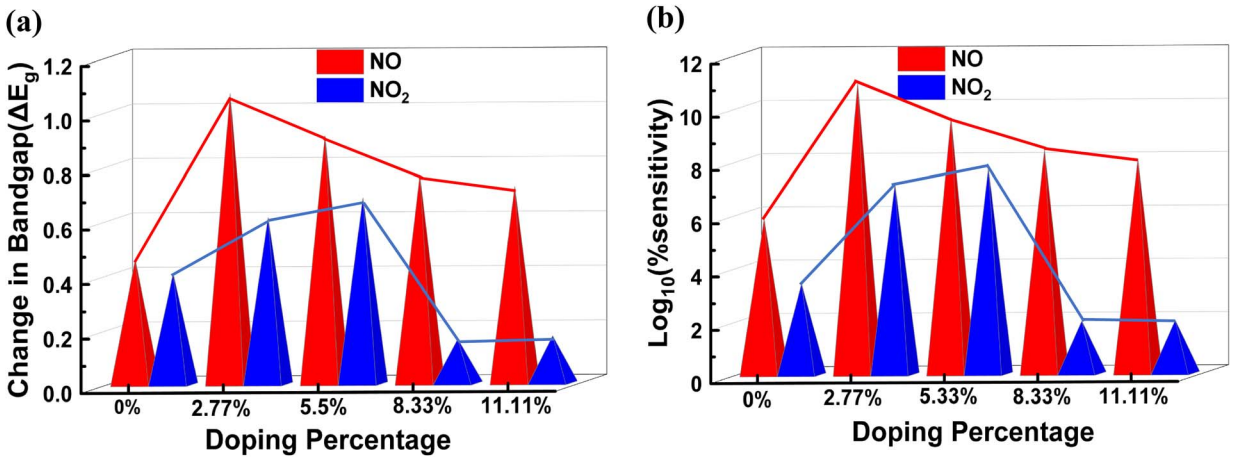

Fig. 9 (a) Change in bandgap *vs.* doping percentage (b) logarithmic sensitivity *vs.* doping percentage.

Table 1 Adsorption energy (E_{ad}), adsorption distance, adsorption sites, bandgap (E_g), charge transfer (ΔQ), change in bandgap of In_2SeTe and Al-doped In_2SeTe monolayer for NH_3, CH_4, CO_2, CO, NO, NO_2 gas molecules

Material	Gas molecules	Suitable sites	Adsorption distance D(Å)	Bandgap (E_g)	Change in bandgap (ΔE_g)	Adsorption energy (E_{ad})	Charge transfer(ΔQ)
In_2SeTe	NH_3	Top of Te	2.86	1.183	−0.009	−0.20	−0.0934
	CH_4	Top of the In–Se bridge	3.27	1.168	−0.024	−0.11	−0.064
	CO_2	Top of the In–Te bridge	3.39	1.115	−0.077	−0.15	−0.039
	CO	Top of in	3.403	1.195	0.003	−0.06	−0.014
	NO	Top of the In–Se bridge	2.17	0.732	−0.460	−0.751	−0.074
	NO_2	Top of the In–Te bridge	2.75	0.784	−0.408	−0.589	−0.066
Al-doped In_2SeTe	NH_3	Top of Te	2.94	1.096	−0.013	−0.225	−0.097
	CH_4	Top of the Al–Se bridge	3.062	1.104	−0.005	−0.129	−0.049
	CO_2	Top of Se	3.31	1.113	−0.004	−0.196	−0.041
	CO	Top of Al	3.8	1.103	−0.006	−0.135	−0.028
	NO	Top of the Al–Se bridge	2.57	0.041	−1.068	−0.774	−0.082
	NO_2	Top of the Al–Te bridge	2.66	0.497	−0.612	−0.701	−0.08

favourable different gas adsorbed structures. From Table 1, it can be clearly seen that among all the gas molecules, NO_x exhibits the maximum adsorption energy, maximum change in bandgap, the shortest adsorption distance, and the largest band gap change in both pristine and Al-doped In_2SeTe monolayers. Although the adsorption energy and charge transfer increase for NO_x after Al doping. Again, the adsorption distance further reduces after Al is introduced. For the pristine In_2SeTe monolayer, the adsorption of NO and NO_2 resulted in adsorption energies of −0.751 eV and −0.589 eV, adsorption distances of 2.17 Å and 2.75 Å, and charge transfers of −0.074|e| and −0.066|e|, respectively. Upon introducing 2.33% Al doping, all these parameters showed noticeable enhancement, with the adsorption energies increasing to −0.774 eV (NO) and −0.701 eV (NO_2), the adsorption distances extending to 2.57 Å and 2.66 Å, and the charge transfers rising to −0.082|e| and −0.080|e|. This suggests that Al doping significantly strengthens the interaction between the monolayer and the NO/NO_2 gas molecules. For other gases, there were no such properties that made them distinguishable. Table 1 represents the selective nature of both pristine and Al-doped In_2SeTe toward NO_x with enhanced sensitivity and selectivity after Al doping.

Table SIV and Table SV provide a detailed summary of the structural parameters for gas adsorption on pristine and Al-doped In_2SeTe. Table SIV lists the adsorption heights of gas molecules and the In–N/O bond lengths for NO and NO_2, while Table SV presents the In–Se/Te bond lengths and the corresponding bond distortions for various adsorbed gases. Together, these tables offer a comprehensive overview of the adsorption geometries, supporting the analysis of gas adsorption performance.

3.5 Chemiresistive sensitivity and recovery characteristics

From Table SVI, the In_2SeTe monolayer with NO and NO_2 adsorption exhibits the largest band gap shift of 0.460 eV and 0.408 eV, respectively, and its sensitivity towards NO and NO_2 is the highest at 7.249958×10^5 and 2.653623×10^5, respectively, in comparison with other gases, which can be observed in Fig. 10. Consequently, after doping, the sensitivity and change in bandgap for NO and NO_2 were 9.17×10^{10}, 1.367×10^7, and

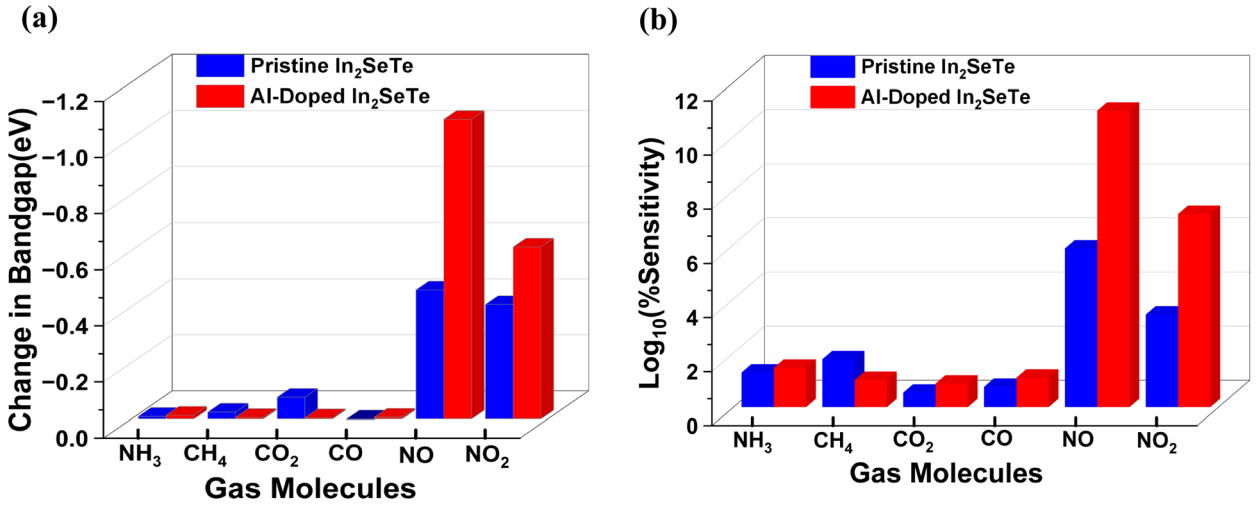

Fig. 10 (a) Comparison of Change in bandgap (ΔE_g) (b) bandgap-based logarithmic sensitivity for different gases after adsorption on In_2SeTe monolayer and Al-doped In_2SeTe monolayer, respectively.

1.068 eV, 0.612 eV, respectively. After analyzing Fig. 10(a) and (b), it can be concluded that doping with Al increases the sensitivity and change in bandgap for NO and NO_2 exceptionally, demonstrating that Al-doping enhances the gas sensing potential of the In_2SeTe monolayer.

The recovery times for various gases at 300 K and 400 K are listed in Table 2, where 300 K is considered room temperature for the calculations. As the temperature increases, the recovery time decreases significantly. At 300 K, NO_x exhibits a relatively long recovery time, indicating strong interaction with both pristine and Al-doped In_2SeTe, making it ideal for room-temperature gas sensing. In contrast, the recovery times for other gases are in the picosecond range, suggesting they desorb too quickly to be effectively detected, thereby limiting their sensing viability. A longer recovery time enhances sensing accuracy. Additionally, Al doping further prolongs the recovery time for NO_x, improving its detection capability and sensor reusability. Thus, both pristine and Al-doped In_2SeTe are promising candidates for NO_x sensing at room temperature.

A comprehensive comparative analysis, presented in Table 3, was performed to assess the gas-sensing capabilities of pristine and Al-doped In_2SeTe monolayers toward NO and NO_2 molecules, alongside eight other structurally similar 2D materials reported in the literature. The evaluation includes critical parameters such as adsorption energy (E_{ad}), charge transfer (ΔQ), recovery time (τ), and sensitivity (S). Both pristine and Al-doped In_2SeTe exhibit outstanding sensitivity levels, even in their undoped form, with the pristine monolayer achieving 7.25 $\times$ 10^5% sensitivity for NO and 2.65 $\times$ 10^5% sensitivity for NO_2. These values already place In_2SeTe among the high-performing materials for gas sensing. However, upon Al doping, the sensing performance experiences a dramatic enhancement. The sensitivity rises by an order of magnitude, reaching 9.17$\times$ 10^{10}% for NO and 1.367 $\times$ 10^7% for NO_2—an exceptional increase that underscores the strong influence of Al dopants in amplifying the surface reactivity and electron interaction of the monolayer. This improvement is further supported by more negative adsorption energies (−0.774 eV for NO and −0.701 eV for NO_2) and higher charge transfer values (0.082e and 0.08 e), compared to the pristine values of −0.751 eV and −0.589 eV with 0.074 e and 0.066 e for NO and NO_2, respectively. Both pristine and Al-doped In_2SeTe have recovery durations that are within a range that is practically feasible, indicating their promise for real-time sensing applications and permitting repeated sensor use. On the other hand, materials such as GaAs have drawbacks. For instance, their incredibly lengthy recovery time (4.45 $\times$ 10^{12} s) makes NO_2 detection difficult and prevents sensor reusability following gas adsorption. Similarly, Ga_2SSe's ultra-short recovery time (6.78 $\times$ 10^{-8} s) leads to fast desorption before effective detection can take place, making NH_3 detection difficult. These materials are not appropriate for accurate gas sensing because of their unfavorable recovery dynamics. The recovery time slightly increases due to stronger molecule binding in the doped system. When benchmarked against eight other 2D gas sensors in Table 3, many of which show lower sensitivity and weaker adsorption interactions, both pristine and especially Al-doped In_2SeTe consistently outperform across all metrics. These results clearly demonstrate that Al doping not

Table 2 In_2SeTe and Al-doped In_2SeTe monolayer recovery time at 300 K for different gas molecules

Gas molecules		NH_3	CH_4	CO_2	CO	NO	NO_2
In_2SeTe	Recovery time(s) at 300 k	2.8557×10^{-9}	6.8872×10^{-11}	6.30623×10^{-9}	1.04426×10^{-11}	4.027	7.7×10^{-3}
Al-doped In_2SeTe		6.138×10^{-9}	1.474×10^{-10}	2.0223×10^{-9}	1.8531×10^{-10}	9.8	0.583

Table 3 Comparison study of sensitivity and recovery time of In_2SeTe and Al-doped In_2SeTe and various other materials

Materials	Sensing gases	%Sensitivity	Recovery time	Adsorption energy (eV)	Charge transfer (e)	Ref.
In_2SeTe	NO_2	2.653623×10^5	7.7×10^{-3}	−0.589	−0.066	This work
	NO	7.249958×10^5	4.027	−0.751	−0.074	
Al doped In_2SeTe	NO_2	1.367×10^7	0.583	−0.701	−0.08	This work
	NO	9.17×10^{10}	9.8	−0.774	−0.082	
GaAs	NO_2	99	4.45×10^{12}	−1.48	0.2803	33
	NO	2.54×10^3	3.52×10^{-6}	−0.4476	−0.18	
In_2SSe	NO_2	3.48×10^3	9.62×10^{-8}	−0.118	−0.665	4
	NH_3	326	3.87×10^{-3}	−0.392	−0.727	
Ga_2SSe	NO_2	1.13×10^{11}	6.41×10^{-7}	−0.167	−1.05	4
	NH_3	590	6.78×10^{-8}	−0.109	−1.04	
MoS_2	NO_2	20	4.32×10^4	−0.208	0.055	34
	NO	NA	NA	−0.138	−0.005	
NbSeTe	NO_2	45	75.74×10^{-6}	−0.59	−0.284	35
	NO	34	17.49×10^{-6}	−0.55	−0.1297	
Pt-doped HfSSe	H_2S	26.3	0.024	−0.614	−0.477	36
	SO_2	70.1	2239.08	−0.918	−0.480	
MoSSe	NO_2	98	2.22×10^2	−0.252	0.137	37
	SO_2	89	1.30	−0.623	0.056	
WSSe	NO_2	NA	4.3×10^{-2}	−0.276	0.122	38
	NO	NA	3.1×10^{-4}	−0.15	0.020	

only enhances the already impressive gas sensing ability of In_2SeTe but also establishes it as a leading-edge material for ultra-sensitive NO and NO_2 detection at room temperature.

3.6 Optical and magnetic properties of pristine and Al-doped In_2SeTe monolayer for NO_x detection

Recent investigations have demonstrated the significant potential of In_2SeTe monolayers for environmental gas sensing through variations in their optical properties. In their pristine form, these monolayers exhibit strong absorption in the ultraviolet (UV) region. Upon the adsorption of gases such as NO, CO, NO_2, and NH_3, distinct and measurable shifts in optical responses occur, enabling the selective detection of these gases. In Fig. S3(a), for the pristine In_2SeTe monolayer, adsorption of NO causes a pronounced shift of the absorption peak toward the near-UV region (~0 nm), resulting in selective near-UV light absorption and making NO uniquely detectable *via* absorption coefficient (AC) analysis. In contrast, CO adsorption leads to a notable increase in the absorption coefficient (~0.58×10^4 cm^{-1}) accompanied by an 18–20 nm blueshift of the absorption peak, indicating a strong optical response. Correspondingly, the refractive index of pristine In_2SeTe in Fig. S3(b) increases significantly by approximately 0.47 at 200 nm after CO adsorption. These changes suggest that pristine In_2SeTe can selectively detect NO and CO gases through combined absorption and refractive index measurements. Upon aluminum doping (Al-doped In_2SeTe monolayer), the optical response shifts, making the material highly selective for NO_2 detection, which can be observed in Fig. 11(a) and (b). Specifically, in Fig. 11(a), the absorption coefficient decreases substantially by about 0.55×10^5 at 270 nm when NO_2 is adsorbed, while other gases induce negligible changes. In Fig. 11(b), the refractive index concurrently decreases by approximately 0.66 with a large redshift of 80 nm, further confirming the selective sensitivity to NO_2. Although CO and NH_3 adsorption cause notable blueshifts in the refractive index peak, their effects are less pronounced compared to NO_2. Thus, Al doping effectively tunes In_2SeTe monolayers for selective NO_2 gas sensing. Overall, these findings highlight that nitrogen-based gas detection is enhanced by aluminum doping, as evidenced by more significant absorption peak shifts and refractive index changes. Pristine In_2SeTe is optimal for selective NO detection, whereas Al-doped In_2SeTe exhibits superior selectivity toward NO_2, making these materials promising candidates for optically based gas sensors in environmental monitoring applications.

The potential of the pristine In_2SeTe monolayer, as well as Al-doped In_2SeTe, as a magnetic gas sensor, has been investigated. The magnetic moment of the gas-adsorbed systems was analyzed using GGA + SOC (spin-unrestricted) computations. When the NO_x molecule was adsorbed, a magnetic moment was induced on the In_2SeTe and Al-doped In_2SeTe monolayer. The separation of the up-spin and down-spin conduction bands in the band structures plot can be observed in Fig. 5(e, f) and 6(e, f). From the figure, it can be inferred that magnetization occurred upon the adsorption of NO_x gases only. As demonstrated in Fig. 11(c, d) and S3(c, d), the induced magnetism was further validated by the asymmetry in the up-spin and down-spin density of the states. The emergence of magnetic moments (0.8 μB to 1.2 μB) in the system occurs only when NO_x molecules are adsorbed onto the surfaces of pristine In_2SeTe or Al-doped In_2SeTe monolayers. The analyte systems In_2SeTe and Al-doped In_2SeTe are non-magnetic in all other gas adsorption situations. The induced magnetic moment is zero μB for these gas adsorbed systems. This unique behavior toward the NO_x molecule suggests that the pristine and Al-doped In_2SeTe monolayer may have potential applications as a magnetic gas sensor for selectively detecting NO_x gases. This enhanced

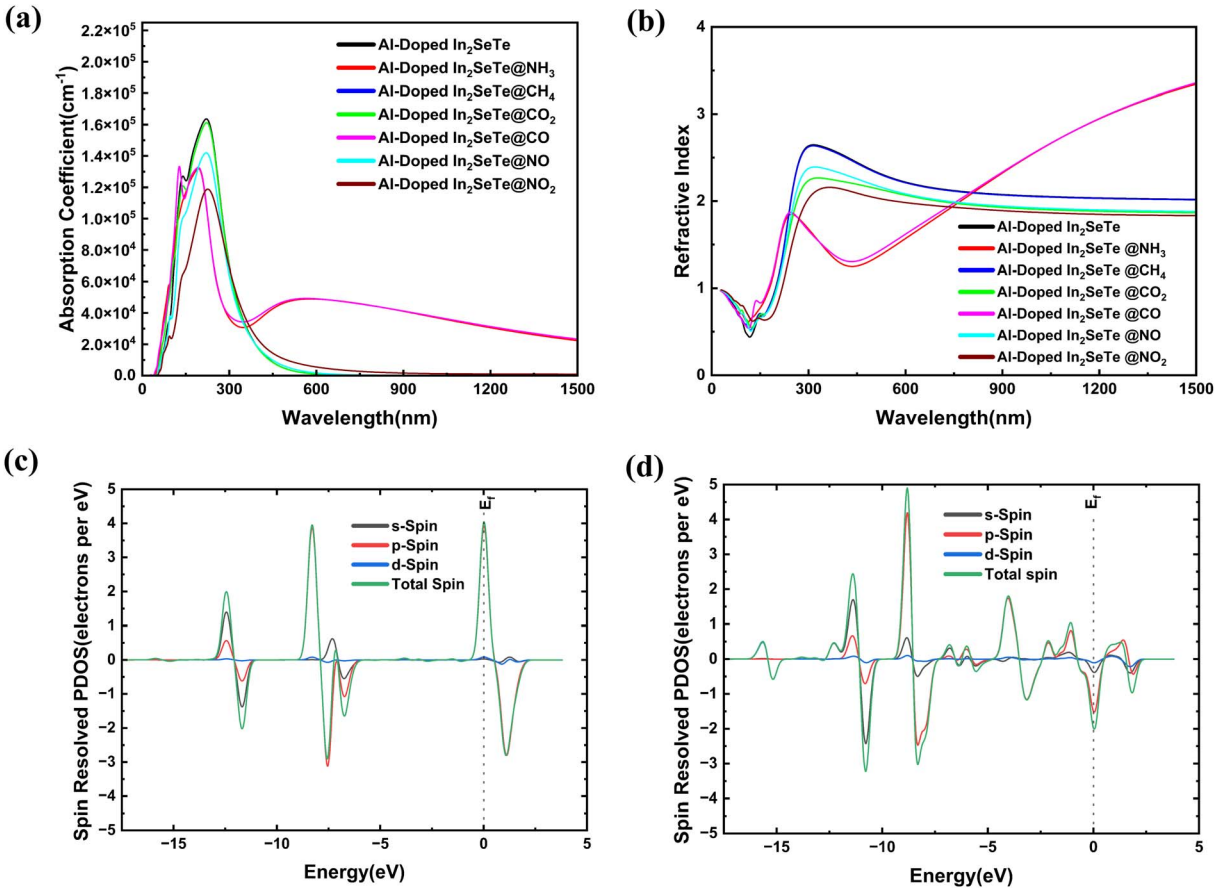

Fig. 11 (a) Absorption coefficient, (b) refractive index of Al-doped In_2SeTe monolayer, spin resolved PDOS of Al-doped In_2SeTe monolayer for (c) NO, (d) NO_2.

selectivity confirms that the magnetic moment in the In_2SeTe-based systems is predominantly influenced by NO_x adsorption, unlike earlier studies where multiple gases contributed, thereby establishing the system's superiority in selective gas detection.

4 Conclusions

In conclusion, a theoretical design of a 2D pristine and Al-doped In_2SeTe monolayer was developed to investigate potential sensor materials for detecting NH_3, CO_2, NO_2, CO, NO, and CH_4 in environmental applications. DFT was employed for geometry optimization to determine the band structure, band gap energy, adsorption distance, charge transfer, lattice constant, DOS, and CDD for NH_3, CO_2, NO_2, CO, NO, and CH_4 molecules on the In_2SeTe monolayer, evaluating its suitability as a gas sensor material. Eventually, it was doped with Al to observe if its properties and sensing capabilities were enhanced. Results showed that both pristine and Al-doped In_2SeTe contain all positive phonon dispersion, making them dynamically stable for gas adsorption. Among all the gases, only the NO and NO_2 gases prefer to be chemisorbed, whereas all other gases prefer to be physisorbed. Additionally, the NO and NO_2 gas molecules adsorbed on the Al-doped In_2SeTe monolayer exhibit the highest adsorption energy and the shortest adsorption distance. The In_2SeTe monolayer was highly selective for NO and NO_2 gases, with sensitivities of 7.249958×10^5 and 2.653623×10^5, which were approximately a million times higher than those of the other gases. Similarly, with Al doping, the sensitivity increases dramatically by 1.26×10^5 and 51.58 times that of the pristine In_2SeTe monolayers, and the sensitivity towards NO and NO_2 becomes 9.17×10^{10} and 1.367×10^7, respectively. The recovery time for both pristine and Al-doped In_2SeTe monolayers remains within a practically acceptable range, demonstrating their suitability for real-time gas sensing applications and ensuring long-term sensor reusability. In addition to baseline performance evaluation, the sensor response was systematically analyzed as a function of Al doping concentration. It was observed that the sensitivity reached its maximum at a critical doping level of 2.33% for NO and 5.5% for NO_2, indicating the existence of optimal doping thresholds for each target gas. Beyond or below these specific doping concentrations, a noticeable decline in sensitivity was recorded, suggesting a delicate balance between structural stability and electronic reactivity introduced by dopant atoms. Optical absorption and refractive–index profiles show that pristine In_2SeTe exclusively senses NO, while Al-doping tailors the monolayer for NO_2 detection. Furthermore, only NO_x

adsorption triggers a magnetic moment in both the undoped and Al-doped sheets, enabling their use as selective magnetic NO_x sensors. This detailed comparison clearly reveals that Al doping significantly enhances the electrical, optical, and chemical properties of the In_2SeTe monolayer. As a result, the Al-doped system exhibits superior selectivity and detection capabilities, positioning it as a highly efficient candidate for advanced gas sensing technologies that aim to detect hazardous environmental gases with high sensitivity and reliability.

Conflicts of interest

All authors declare that they have no conflict of interest.

Data availability

The data supporting this article have been included as part of the Supplementary Information (SI). Supplementary information: the structural, electronic, and adsorption properties of pristine and Al-doped In_2SeTe monolayers, including calculated lattice constants, bond lengths, bond angles, layer thickness, band gaps, VBM/CBM positions, and dynamic stability (Table SI), alongside a comparison with previous theoretical studies validating the computational results (Table SII). It presents optimized adsorption structures and charge-density difference maps for NH_3, CH_4, CO_2, CO, NO, and NO_2 molecules on In_2SeTe (Fig. S1 and S2), as well as the effect of Al doping on band gap and gas-sensing sensitivity across different concentrations (Table SIII). Gas adsorption parameters such as adsorption heights, In–N/O bond lengths, and In–Se/Te bond distortions for NO and NO_2 on pristine and doped surfaces are summarized (Tables SIV and SV), indicating interaction strengths and structural deformation. Finally, optical properties including absorption coefficient, refractive index, and spin-resolved partial density of states of pristine In_2SeTe, with and without NO and NO_2 adsorption, are reported (Fig. S3). See DOI: **https://doi.org/10.1039/d5ra05591a**.

Acknowledgements

We would like to express our sincere gratitude to the Department of Electrical and Electronic Engineering, Khulna University of Engineering & Technology (KUET), Khulna-9203, Bangladesh, for their continuous support and encouragement throughout this research. This work was supported by the UGC Funded Research Project 2024–2025. We also acknowledge the valuable software and technical support provided by the Central Computer Centre, Khulna University of Engineering & Technology (KUET), Khulna-9203, Bangladesh.

References

1 D. Ma, *et al.*, C_3N monolayers as promising candidates for NO_2 sensors, *Sens. Actuators, B*, 2018, **266**, 664–673, DOI: **10.1016/j.snb.2018.03.159**.
2 Q. Wu, L. Cao, Y. S. Ang and L. K. Ang, Superior and tunable gas sensing properties of Janus PtSSe monolayer, *Nano Express*, 2020, **1**(1), 010042, DOI: **10.1088/2632-959X/ab95e6**.
3 L. Wan, D. Chen, W. Zeng, J. Li and S. Xiao, Hazardous gas adsorption of Janus HfSeTe monolayer adjusted by surface vacancy defect: A DFT study, *Surf. Interfaces*, 2022, **34**, 102316, DOI: **10.1016/j.surfin.2022.102316**.
4 K. A. Abdur Nur, M. S. Hasan Khan and M. R. Islam, Superior selectivity for NH_3 (NO_2) gas molecules in In_2SSe (Ga_2SSe) Janus materials: a first-principles study, *Phys. Scr.*, 2024, **99**(9), DOI: **10.1088/1402-4896/ad69d2**.
5 S. Sucharitakul, *et al.*, Intrinsic Electron Mobility Exceeding 103 cm2/(V s) in Multilayer InSe FETs, *Nano Lett.*, 2015, **15**(6), 3815–3819, DOI: **10.1021/acs.nanolett.5b00493**.
6 A. Kandemir and H. Sahin, Janus single layers of In_2SSe: A first-principles study, *Phys. Rev. B*, 2018, **97**(15), DOI: **10.1103/PhysRevB.97.155410**.
7 C. Wang, C. Gao, J. Hou and Q. Duan, First-principle investigation of CO, CH4 and CO2 adsorption on Cr-doped graphene-like hexagonal borophene, *J. Mol. Model.*, 2022, **28**, 196, DOI: **10.21203/rs.3.rs-1456018/v1**.
8 Selective and sensitive toxic gas-sensing mechanism in a 2D Janus MoSSe monolayer.
9 S. Saha, D. I. Sajib and M. K. Alam, Interaction of the III-As monolayer with SARS-CoV-2 biomarkers: implications for biosensor development, *Phys. Chem. Chem. Phys.*, 2024, **26**(7), 6242–6255, DOI: **10.1039/d3cp05215j**.
10 H. Cui, M. Ran, X. Peng and G. Zhang, First-principles design of noble metal (Rh and Pd) dispersed Janus WSTe monolayer for toxic gas sensing applications, *J. Environ. Chem. Eng.*, 2024, **12**(2), 112047, DOI: **10.1016/j.jece.2024.112047**.
11 A. Y. Lu, *et al.*, Janus monolayers of transition metal dichalcogenides, *Nat. Nanotechnol.*, 2017, **12**(8), 744–749, DOI: **10.1038/nnano.2017.100**.
12 Y. Guo, S. Zhou, Y. Bai and J. Zhao, Defects and oxidation of group-III monochalcogenide monolayers, *J. Chem. Phys.*, 2017, **147**(10), DOI: **10.1063/1.4993639**.
13 S. Pal Kaur, T. Hussain and T. J. Dhilip Kumar, Substituted 2D Janus WSSe monolayers as efficient nanosensor toward toxic gases, *J. Appl. Phys.*, 2021, **130**(1), DOI: **10.1063/5.0054319**.
14 D. Wang, *et al.*, Janus MoSSe monolayer: A highly strain-sensitive gas sensing material to detect SF_6 decompositions, *Sens. Actuators, A*, 2020, **311**, DOI: **10.1016/j.sna.2020.112049**.
15 L. Zhang, *et al.*, Recent advances in emerging Janus two-dimensional materials: From fundamental physics to device applications, *J. Mater. Chem. A*, 2020, **8**(18), 8813–8830, DOI: **10.1039/d0ta01999b**.
16 R. Chaurasiya and A. Dixit, Defect engineered MoSSe Janus monolayer as a promising two dimensional material for NO_2 and NO gas sensing, *Appl. Surf. Sci.*, 2019, **490**, 204–219, DOI: **10.1016/j.apsusc.2019.06.049**.
17 P. Yu, *et al.*, Pd doped Janus HfSeS monolayer: Ultrahigh sensitive gas sensing material for reversible detection of

NO, *Sens. Actuators, A*, 2024, **365**, 114864, DOI: 10.1016/j.sna.2023.114864.

18 A. Marjaoui, M. Zanouni, M. Ait Tamerd, A. El Kasmi and M. Diani, A First-Principles Investigation on Electronic Structure, Optical and Thermoelectric Properties of Janus In_2SeTe Monolayer, *J. Supercond. Novel Magn.*, 2021, **34**(12), 3279–3290, DOI: 10.1007/s10948-021-06028-0.

19 R. Shahriar, O. Hassan and M. K. Alam, Adsorption of gas molecules on buckled GaAs monolayer: a first-principles study, *RSC Adv.*, 2022, **12**(26), 16732–16744, DOI: 10.1039/d2ra02030k.

20 H. Chen, *et al.*, Exploring monolayer Janus MoSSe as potential gas sensor for Cl2, H2S and SO2, *Comput. Theor. Chem.*, 2022, **1211**, 113665, DOI: 10.1016/j.comptc.2022.113665.

21 H. T. T. Nguyen, *et al.*, Spin-orbit coupling effect on electronic, optical, and thermoelectric properties of Janus Ga2SSe, *RSC Adv.*, 2020, **10**(73), 44785–44792, DOI: 10.1039/d0ra08279a.

22 M. Bala, M. T. Rahman, R. Al Nahean and M. S. Hasan Khan, NO_2 and SO_2 adsorption and sensing on Janus B_2SeTe: unveiling its electronic, optical, and magnetic properties through DFT and COMSOL, *RSC Adv.*, 2025, **15**(31), 25187–25201, DOI: 10.1039/D5RA04190B.

23 A. Salehi and D. Jamshidi Kalantari, Characteristics of highly sensitive Au/porous-GaAs Schottky junctions as selective CO and NO gas sensors, *Sens. Actuators, B*, 2007, **122**(1), 69–74, DOI: 10.1016/j.snb.2006.05.004.

24 B. Zhu, *et al.*, Monolayer Janus Te_2Se-based gas sensor to detect $SO_2$and NOx: A first-principles study, *Phys. Chem. Chem. Phys.*, 2021, **23**(2), 1675–1683, DOI: 10.1039/d0cp05750a.

25 R. Shahriar, O. Hassan and M. K. Alam, Adsorption of gas molecules on buckled GaAs monolayer: a first-principles study, *RSC Adv.*, 2022, **12**(26), 16732–16744, DOI: 10.1039/d2ra02030k.

26 C. Jin, X. Tang, X. Tan, S. C. Smith, Y. Dai and L. Kou, A Janus MoSSe monolayer: a superior and strain-sensitive gas sensing material, *J. Mater. Chem. A*, 2019, **7**(3), 1099–1106, DOI: 10.1039/C8TA08407F.

27 P. Panigrahi, D. Jini, H. Bae, H. Lee, R. Ahuja and T. Hussain, Two-dimensional Janus monolayers of MoSSe as promising sensor towards selected adulterants compounds, *Appl. Surf. Sci.*, 2021, **542**, 148590, DOI: 10.1016/j.apsusc.2020.148590.

28 L. Wan, D. Chen, W. Zeng, J. Li and S. Xiao, Hazardous gas adsorption of Janus HfSeTe monolayer adjusted by surface vacancy defect: A DFT study, *Surf. Interfaces*, 2022, **34**, 102316, DOI: 10.1016/j.surfin.2022.102316.

29 H. Zhao, *et al.*, Janus In_2SeTe for photovoltaic device applications from first-principles study, *Chem. Phys.*, 2022, **553**, DOI: 10.1016/j.chemphys.2021.111384.

30 D. Xu, B. Cai, J. Tan and G. Ouyang, Tailoring the anisotropic effect of Janus In_2XY (X/Y = S, Se, Te) monolayers toward realizing multifunctional optoelectronic device applications, *New J. Phys.*, 2023, **25**(8), DOI: 10.1088/1367-2630/ace845.

31 T. V. Vu, *et al.*, Electronic, optical, and thermoelectric properties of Janus In-based monochalcogenides, *J. Phys. Condens. Matter*, 2021, **33**(22), DOI: 10.1088/1361-648X/abf381.

32 M. Bala, M. T. Rahman, R. Al Nahean, B. Sorker, and M. R. Firoz, Adsorption and Gas Sensing Properties of GaAs Monolayer: A DFT Study, in *13th International Conference on Electrical and Computer Engineering, ICECE 2024*, Institute of Electrical and Electronics Engineers Inc., 2024, pp. 74–79, DOI: 10.1109/ICECE64886.2024.11024722.

33 R. Shahriar, O. Hassan and M. K. Alam, Adsorption of gas molecules on buckled GaAs monolayer: a first-principles study, *RSC Adv.*, 2022, **12**(26), 16732–16744, DOI: 10.1039/d2ra02030k.

34 X. Tian, *et al.*, Recent advances in MoS_2-based nanomaterial sensors for room-temperature gas detection: A review, *Sens. Diagn.*, 2023, **2**(2), 361–381, DOI: 10.1039/d2sd00208f.

35 D. Singh and R. Ahuja, Highly sensitive gas sensing material for environmentally toxic gases based on Janus NbSeTe monolayer, *Nanomaterials*, 2020, **10**(12), 1–17, DOI: 10.3390/nano10122554.

36 J. Hu, Q. Zhang, Q. Zhang and H. Cui, Favorable sensing property of Pt-doped Janus HfSSe monolayer upon H_2S and SO_2: A first-principles theory, *J. Mater. Res. Technol.*, 2022, **20**, 763–771, DOI: 10.1016/j.jmrt.2022.07.080.

37 B. Babariya, D. Raval, S. K. Gupta and P. N. Gajjar, Selective and sensitive toxic gas-sensing mechanism in a 2D Janus MoSSe monolayer, *Phys. Chem. Chem. Phys.*, 2022, **24**(25), 15292–15304, DOI: 10.1039/d2cp01648f.

38 R. Chaurasiya and A. Dixit, Ultrahigh sensitivity with excellent recovery time for $NH_3$and NO_2in pristine and defect mediated Janus WSSe monolayers, *Phys. Chem. Chem. Phys.*, 2020, **22**(25), 13903–13922, DOI: 10.1039/d0cp02063j.